

STUDY OF INSTALLATION EFFECTS ON A HIGH-LIFT WING SECTION IN AN OPEN WIND TUNNEL

Lars Tysell

FOI, Swedish Defence Research Agency

Keywords: *High-lift, wing section, wind tunnel, viscous computations, grid generation*

Abstract

In this work the installation effects on a high-lift wing section with endplates in a wind tunnel have been studied. The test section in the tunnel is open, with a complex bar and strut setup to hold the wing section including the endplates. Thus the flow around the wing section and in the wind tunnel is very complex, with possibly large influence of the experimental setup. The three-dimensional effects has also been studied by computations on the wing section in free flight and by comparison with two-dimensional computations.

1 Introduction

Within the European 7th framework program project SADE smart high lift devices have been studied. The studied configuration is a wing section with a flexible wing leading edge and a trailing edge flap, studied both by computations and experiments in a wind tunnel. The work done by FOI cover the computational study of the wind tunnel installation effects.

2 Computational tools

The flow solver EDGE, described in [1], has been used for the flow computations. It solves the compressible Reynolds Averaged Navier-Stokes (RANS) equations. The solver is a node-centered edge-based finite volume solver for arbitrary grid elements. The finite volume scheme is applied on the dual grid. The governing equations are integrated explicitly towards steady state with

Runge-Kutta time integration. The convergence is accelerated with an agglomeration multigrid technique and implicit residual smoothing. Several turbulence models can be chosen. The EARSM turbulence model [2] is one of them.

The grid generator TRITET, described in [3] and [4] for generation of unstructured/hybrid grids in two and three dimensions has been used for the grid generation. The input is the surface patch definition. The main algorithms for the grid generation is the advancing front algorithm for the unstructured part and an advancing layer algorithm for the prismatic part.

3 Studied configuration

The studied configuration is a wing section of a high-lift configuration, with one flap and a drooped nose. The experimental setup in the Tsagi open wind tunnel T-101 can be seen in Figure 1. The elliptic cross section of the tunnel is 24×14 m. The geometry can be seen in Figure 2. In order to make the flow more like a two-dimensional flow, for which the configuration was designed, endplates were placed at both sides of the wing section. The endplates were designed by DLR [5]. That study showed the endplates needed to be much bigger, in order to get a more two-dimensional flow, than was feasible to use in the experiment. The chord for the configuration with the flap retracted is 3.0 m with a span of 5.0 m.

4 Computational results

The computations were done at $U_\infty = 40.0$ m/s, i.e. $M_\infty = 0.1176$ and $Re_c = 8,209,000$ with chord taken for the flap in retracted position.

4.1 Two-dimensional computations

The configuration was first studied in 2D. The hybrid grid for this configurations is shown in Figure 2. The grid has about 55,000 points including 45 prismatic layers. The first grid layer has a thickness of about $y^+ = 1.0$. The EARSM turbulence model has been used. 20 computations were done, with angle of attack from 0.0° to 19.0° . The results are shown in Figure 6. It can be seen that the CL curve is linear up to about 10.0° angle of attack with CL_{max} at 13.0° angle of attack.

4.2 Three-dimensional computations

The 3D configuration in the wind tunnel is shown in Figure 1. The complete configuration consists of about 440 surface patches. As can be seen the experimental setup is very complex with several struts and bars. To do computations at different angles of attack would require different grids, with modification of the geometry for each angle of attack. Thus, only one angle of attack was chosen to be studied in this work. The angle of attack at 10.0° , which is right after the linear region in Figure 6, was chosen. The surface grid is shown in Figure 3 - Figure 5. The grid has about 8,800,000 points, including 45 prismatic layers. The first grid layer has a thickness of about $y^+ = 1.0$. As can be seen in Figure 5 stretched elements have been generated at regions of high curvature in order to reduce the number of grid points. The result of the computation, using the Spalart-Allmaras turbulence model, is shown in Figure 6. In this figure it can be seen that the result differs very much from the 2D results. CL is much lower than in the results in 2D.

Due to the large difference in CL , computations have also been made for the wing section including the endplates in free flight, i.e. not in the wind tunnel. For the 3D configuration in free

flight computations have been done for six angle of attacks up to 25.0° , for the Spalart-Allmaras turbulence model. The results are shown in Figure 6, where it can be seen that CL_{max} is never reached. The behaviour of the $CL(\alpha)$ curve is completely linear, which is very different from the results in 2D. A thorough investigation of the difference between the 2D and 3D results is given in [5], giving similar results as here. It can also be seen that the lift is about 8.0% lower for the computations in the wind tunnel than in free flight. This is probably due to a non-perfect setting of the flow condition and reference quantities, see the discussion about Figure 11 below.

The result for the configuration in the wind tunnel at different span stations are shown in Figure 7. Span station $y=0.0$ m is at midspan. It can be seen that the results at the different span stations are almost the same. So the difference between the 2D and 3D results is not because of a varying span loading for the 3D case. Instead the loading has been lowered with about the same magnitude all over the span.

The streamlines for the configuration in the wind tunnel are shown in Figure 8. The separated areas at an angle of attack of 10.0° for the configuration in free flight and the configuration in the wind tunnel are shown in Figure 9. It can be seen that the separated areas are similar.

Figure 10 shows the C_p distribution at an angle of attack 10.0° for both the 2D configuration and the configuration in the wind tunnel. It can be seen that the C_p distributions are very different. The pressure peak at the leading edge for the 2D configuration is not present for the configuration in the wind tunnel. Figure 10 also shows the C_p distribution at angle of attack 0.0° for the 2D configuration and the C_p distribution at angle of attack 10.0° for the configuration in the wind tunnel. These two C_p distributions match better. So it may be concluded that the result for the configuration in the wind tunnel approximately corresponds to the result in 2D for an angle of attack that is more than 10.0° lower.

Figure 11 shows a comparison for the C_p distribution between the configuration in the wind tunnel and the configuration in free flight. It can be seen that there is a difference. This could also

be seen earlier in Figure 6. Despite the setting of the flow condition in the tunnel has been set as best as possible to be equal to the condition in free flight, there might be a small difference in the setting. The computation in free flight is done with a homogenous flow upstream of the geometry, which is not the case for the WT case. The flow at the inlet is not homogenous. So it is not clear how to set the condition in order to get the flow most similar to the condition for the free flight case. With a small change in the reference static and dynamic pressure the curves can be set to match exactly, as can be seen in the right figure. Here the reference static pressure was increased by 0.05% and the dynamic pressure was reduced by 8.0%. This corresponds to a change of the freestream velocity by 4.0%. By this modifications it can be seen that the C_p distributions are almost identical. This modification will also remove the difference in CL in Figure 6.

Figure 12 shows a comparison for the C_p distribution between the configuration in the wind tunnel and the experimental results at a cut at $y=0.0$ m and a cut at 1.75 m. The first cut is at mid span. The results are similar but there is a difference in the level. This may be explained by the above discussion of reference values, since how this is done may be different.

Figure 13 shows Mach number and streamlines for angle of attack 0.0° for the 2D configuration, whereas Figure 14 shows Mach number and streamlines for angle of attack 10.0° . Figure 15 show Mach number and streamlines for angle of attack 10.0° for the 3D configuration in free flight, whereas Figure 16 shows Mach number and streamlines for angle of attack 10.0° for the 3D configuration in the wind tunnel. It can be seen that the downwash behaviour for the 3D configuration in free flight for the angle of attack 10.0° is more similar to the behaviour at the angle of attack 10.0° for the 2D configuration than at the angle of attack 0.0° , but the Mach number distribution around the wing is more similar to the 2D configuration for the angle of attack 0.0° . It can also be seen that the flow for the 3D configuration in the wind tunnel is similar to the flow for the 3D configuration in free flight, but one difference is that some of the flow go below the out-

let of the tunnel, as can be seen in Figure 16. This can also be seen in Figure 17, where we see the Mach number at a cut right after the inlet, and right before the outlet, respectively. Figure 18 shows there is no downwash for the 3D configuration in the tunnel if the wing is removed, so the flow going below the outlet is clearly caused by the wing. This could probably have been eliminated by placing the wing section at a higher position.

5 Conclusion

The installation effects on a high-lift wing section in an open wind tunnel has been studied by viscous computations. A large effort was made to generate the grid for this configuration. The computations show that the results in the wind tunnel differ very much from the 2D computations. The configuration in the wind tunnel never reach CL_{max} , as in the 2D computations, despite the use of large endplates. The computations show that the main reason for the difference is not coming from the wind tunnel setup, but instead from 3D effects, caused by a short wing span. The use of the endplates only have a very limited effect on the 3D results. When doing computations in an open wind tunnel it is also important to set correct values on the reference quantities in order to get good agreement with the geometry in free flight.

Acknowledgment

This work has been performed within the scope of the SADE project funded by the European 7th framework programme. The Author thank DLR for the geometry definition of the wing section with endplates and Tsagi for the geometry definition of the wind tunnel and the wind tunnel measurements.

References

- [1] Eliasson, P., EDGE, a Navier-Stokes Solver for Unstructured Grids. Proceedings of Finite Volumes for Complex Applications III, ISBN 1-9039-9634-1, pp. 527-534, 2002.
- [2] Wallin S. and Johansson A. V. An Explicit Algebraic Reynolds Stress Model of Incompressible

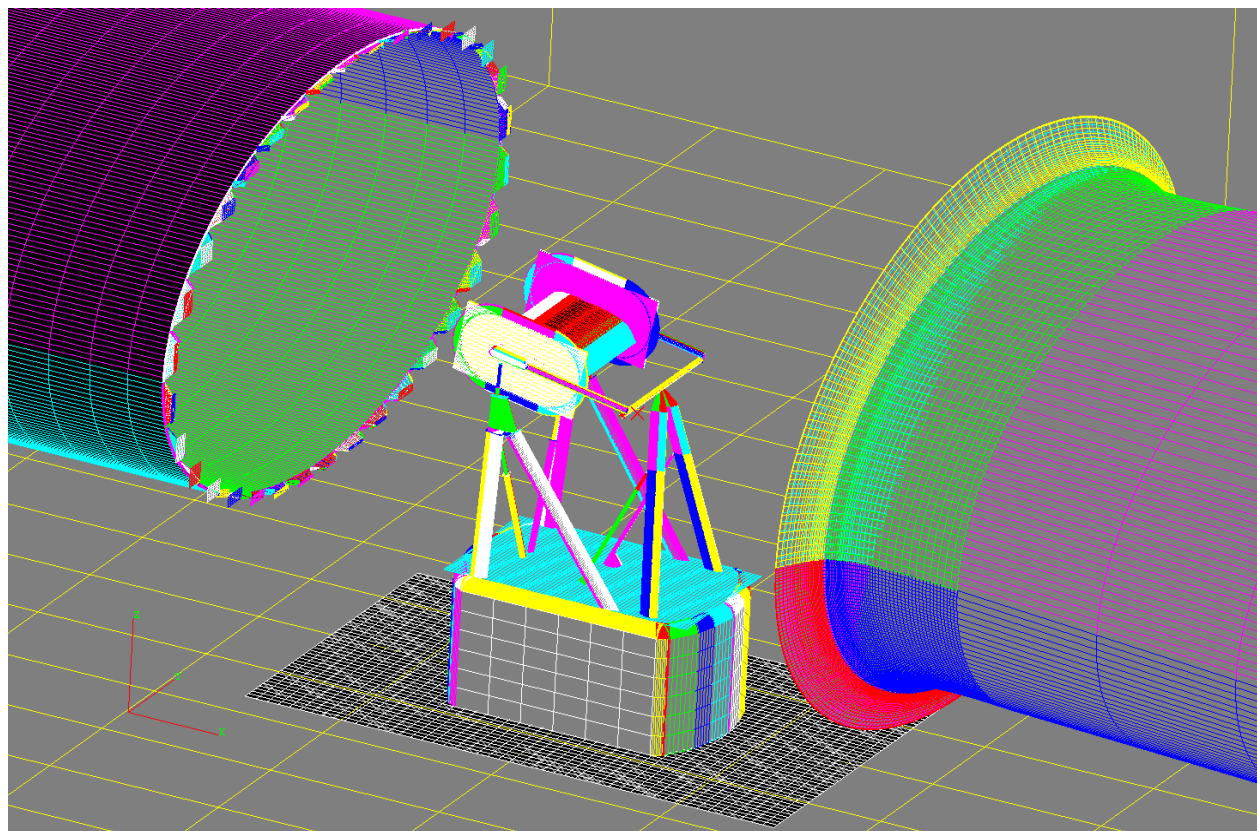


Fig. 1 Surface patches for the wing section in the wind tunnel.

and Compressible Flows. *Journal of Fluid Mechanics* Vol. 403, pp 89-132, 2000.

- [3] Tysell, L., An Advancing Front Grid Generation System for 3D Unstructured Grids. ICAS Paper ICAS-94-2.5.1, pp. 1552-1564, Anaheim, California, USA, 1994.
- [4] Tysell, L., Hybrid Grid Generation for Complex 3D Geometries. Proceedings of the *7th International Conference on Numerical Grid Generation in Computational Field Simulations*, pp. 337-346, International Society of Grid Generation (ISGG), Whistler, British Columbia, Canada, 2000.
- [5] Kühn, T. and Lenfers, C., A Numerical Assessment of Side Plate Effects for a Low Aspect Ratio Wind Tunnel Model with a Smart Droop Nose Device, AIAA 2012-3021, *30th AIAA Applied Aerodynamics Conference*, New Orleans, USA, 2012.

Copyright Statement

The authors confirm that they, and/or their company or organization, hold copyright on all of the original material included in this paper. The authors also confirm that they have obtained permission, from the copyright holder of any third party material included in this paper, to publish it as part of their paper. The authors confirm that they give permission, or have obtained permission from the copyright holder of this paper, for the publication and distribution of this paper as part of the ICAS 2014 proceedings or as individual off-prints from the proceedings.

STUDY OF INSTALLATION EFFECTS ON A HIGH-LIFT WING SECTION

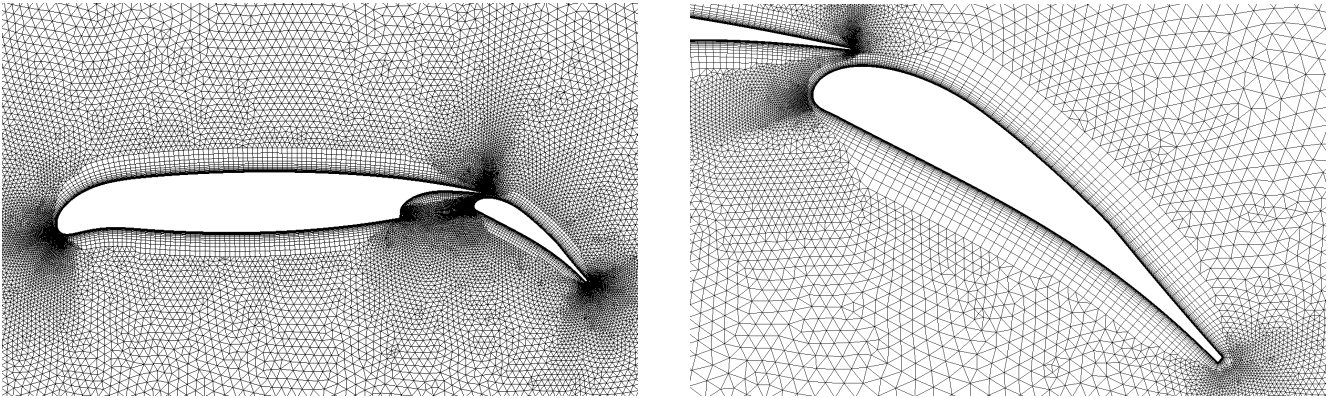


Fig. 2 Hybrid grid for the droop nose configuration with the flap in landing position.

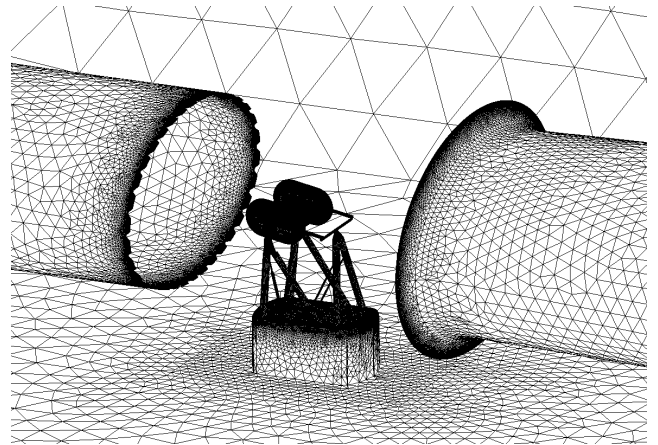
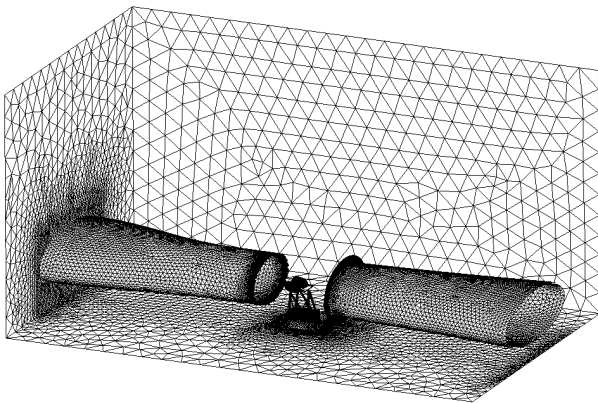


Fig. 3 Surface grid for the wing section in the wind tunnel. The front and backside walls are not shown in the figure.

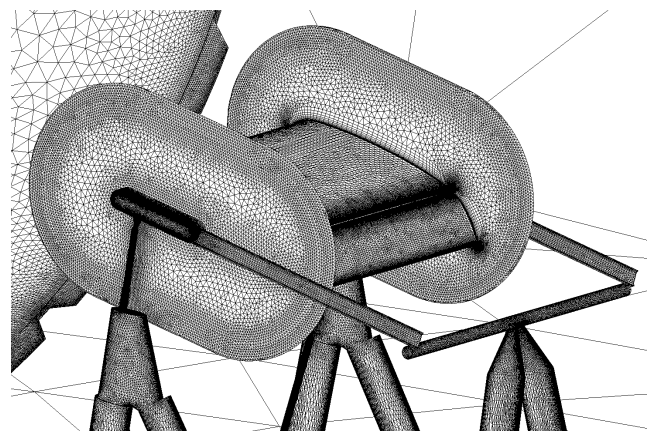
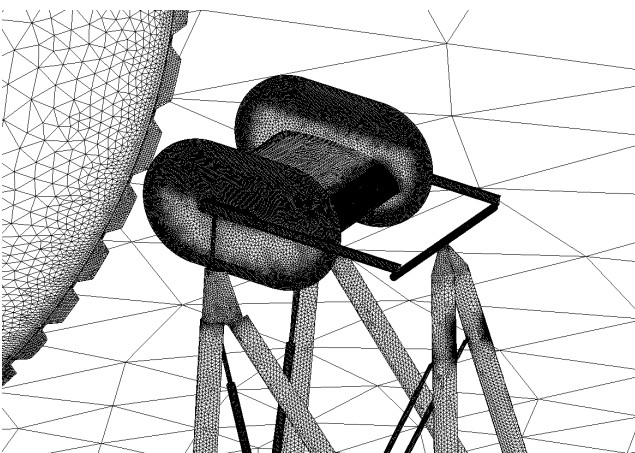


Fig. 4 Surface grid for the wing section in the wind tunnel.

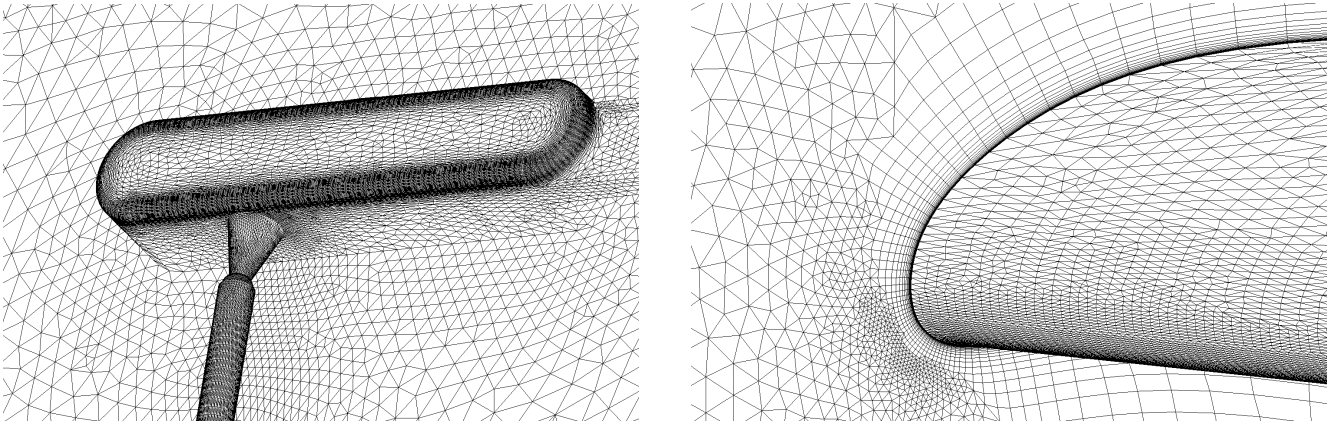


Fig. 5 Surface grid for the wing section in the wind tunnel. Even the struts and the ball joints are modeled in detail.

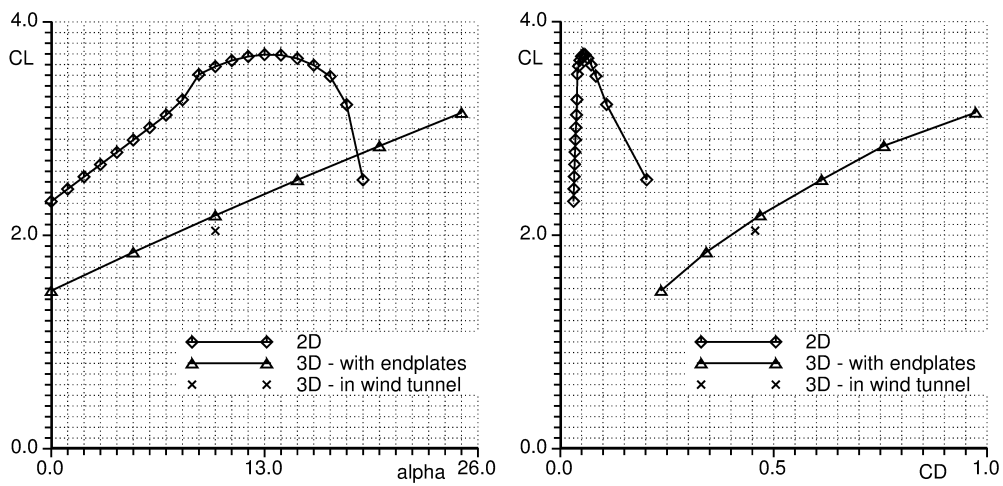


Fig. 6 $CL(\alpha)$ and $CL(CD)$ for the 2D case, the 3D free flight case with endplates and the WT case. Landing flap + droop nose configuration.

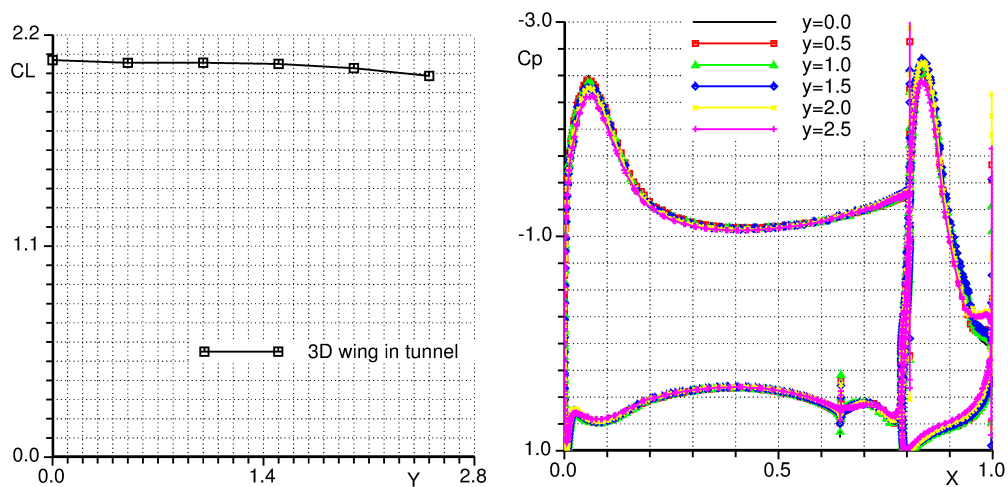


Fig. 7 Loading and $C_p(x)$ for different span cuts for the WT case.

STUDY OF INSTALLATION EFFECTS ON A HIGH-LIFT WING SECTION

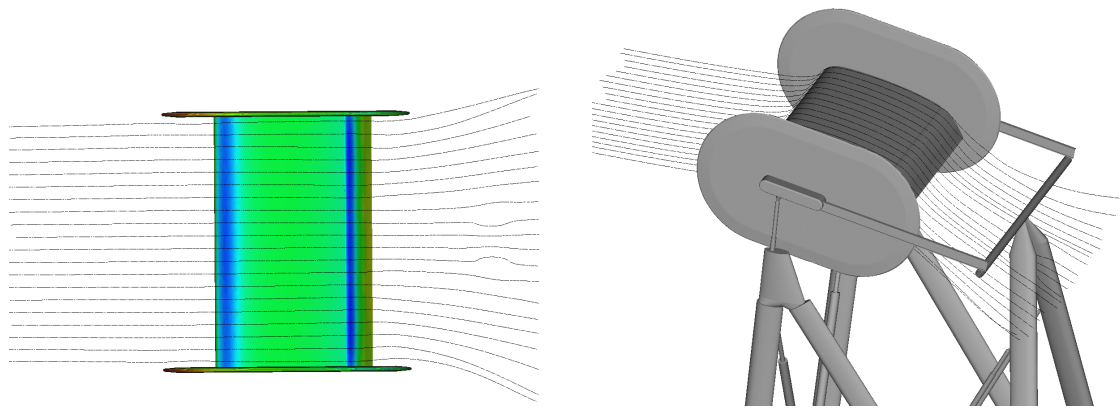


Fig. 8 Streamlines and C_p (scale = [-2.5,1.0]) for the WT case at $AoA=10.0^\circ$.

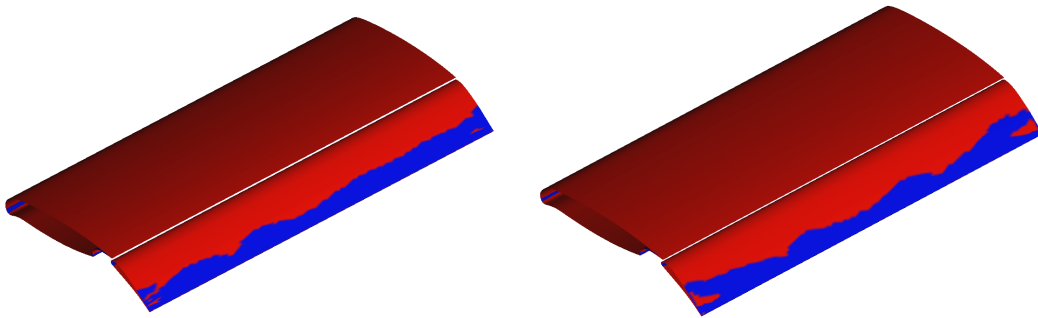


Fig. 9 Separated areas for the 3D free flight case (left) at $AoA=10.0^\circ$ and the WT case (right) at $AoA=10.0^\circ$.

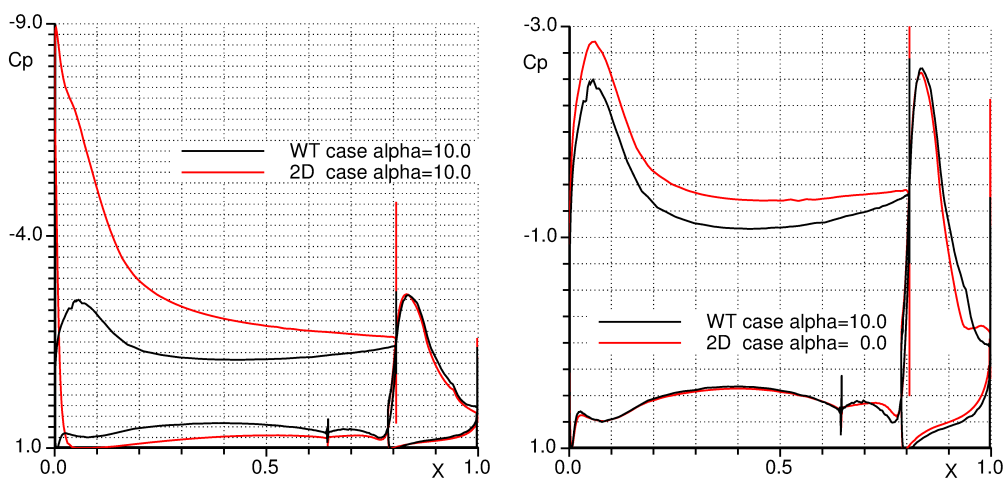


Fig. 10 $C_p(x)$ for the 2D case at $AoA=10.0^\circ$ and the WT case at $AoA=10.0^\circ$ (left) and the 2D case at $AoA=0.0^\circ$ and the WT case at $AoA=10.0^\circ$ (right).

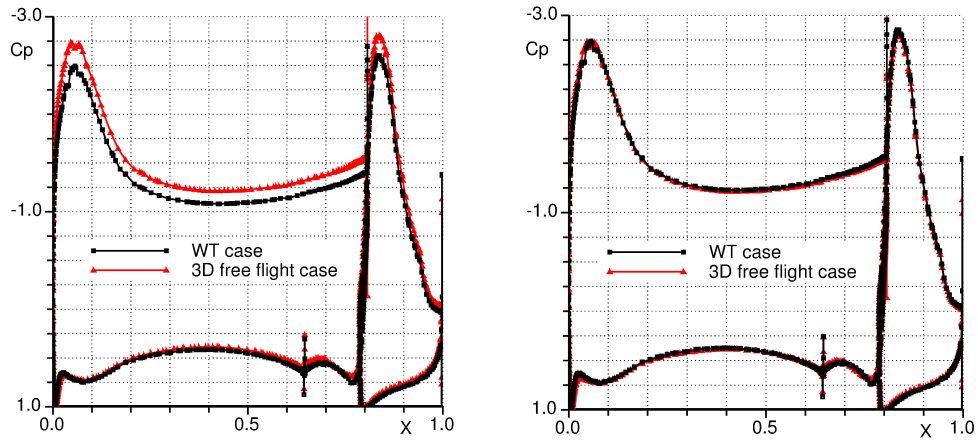


Fig. 11 $C_p(x)$ for the WT case and the 3D free flight case at $AoA=10.0^\circ$ at span station $y=0.0$ m. With originally selected static/dynamic reference pressures for the WT case (left) and with modified static/dynamic reference pressures (right).

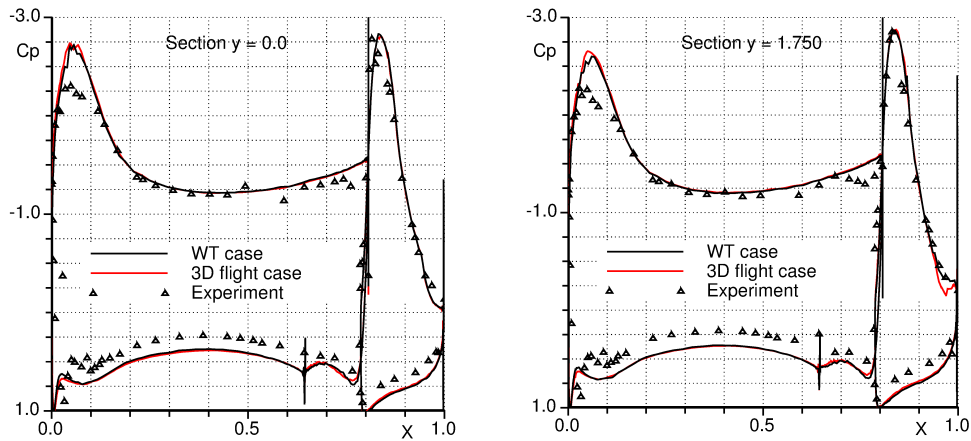


Fig. 12 $C_p(x)$ for the WT case, 3D free flight case and experiment at $AoA=10.0^\circ$ at span stations $y=0.0$ m and $y = 1.750$ m. With modified static/dynamic reference pressures for the WT case.

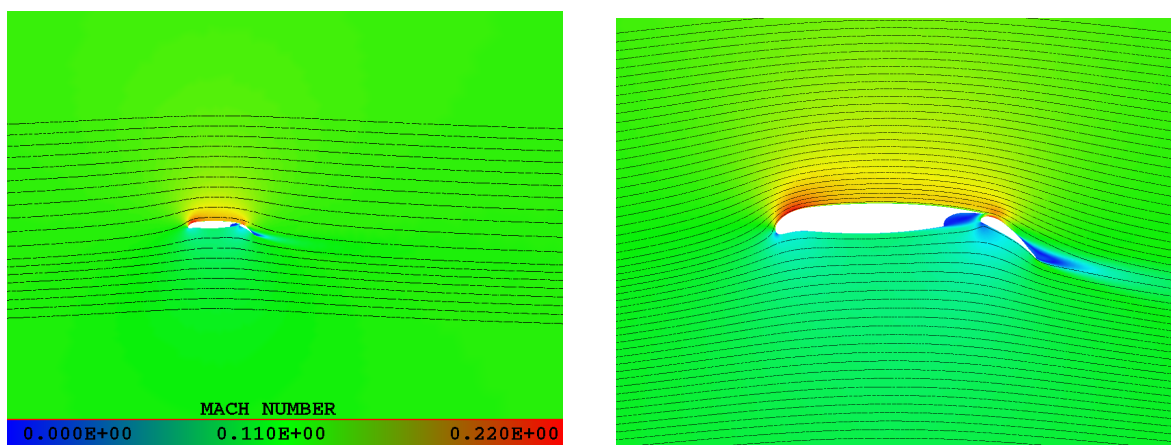


Fig. 13 Mach number and streamlines for the 2D case at $AoA=0.0^\circ$.

STUDY OF INSTALLATION EFFECTS ON A HIGH-LIFT WING SECTION

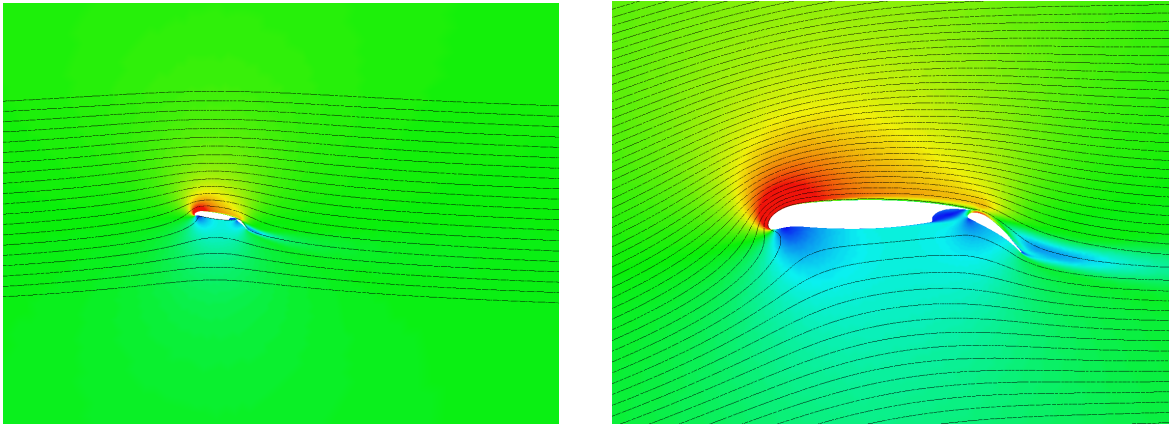


Fig. 14 Mach number and streamlines for the 2D case at $AoA=10.0^\circ$.

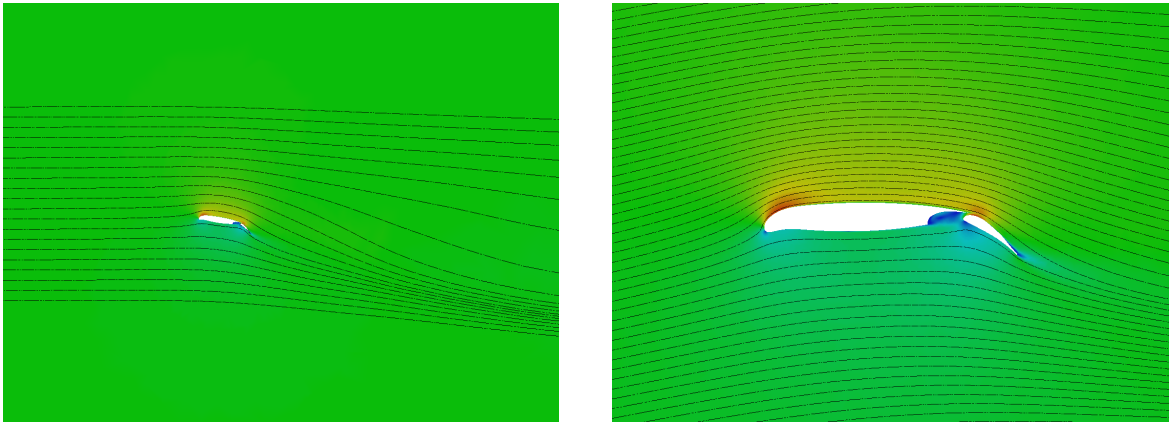


Fig. 15 Mach number and streamlines for the 3D free flight case at $AoA=10.0^\circ$ at span station $y=0.0$ m.

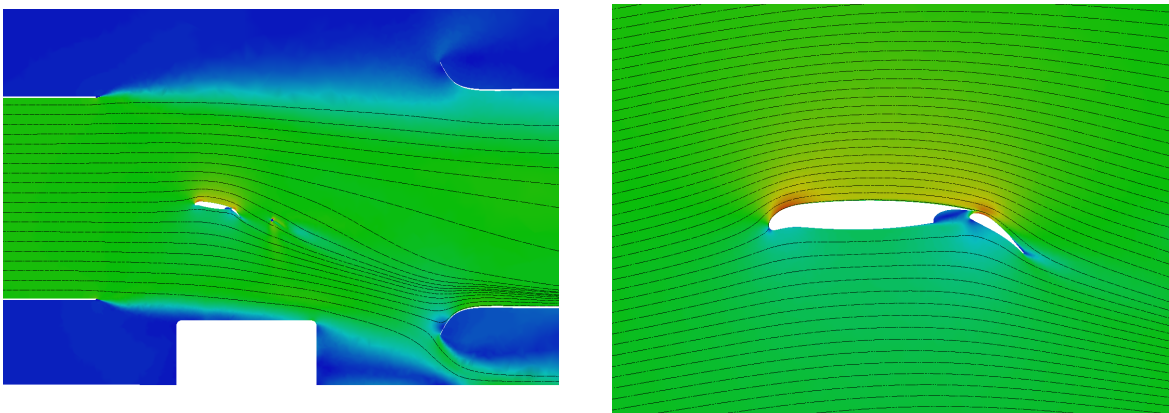


Fig. 16 Mach number and streamlines for the WT case at $AoA=10.0^\circ$ at span station $y=0.0$ m.

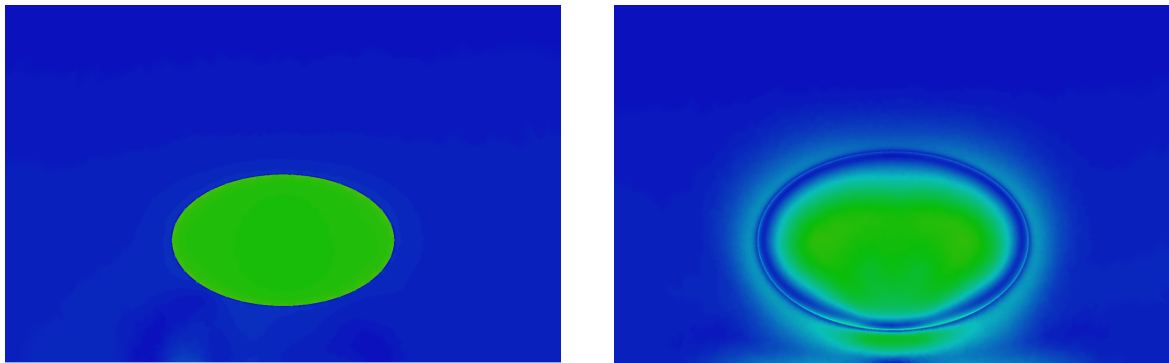


Fig. 17 Mach number for the WT case at $AoA=10.0^\circ$ at inlet at station $x=10.695$ m and outlet at station $x=13.575$ m.

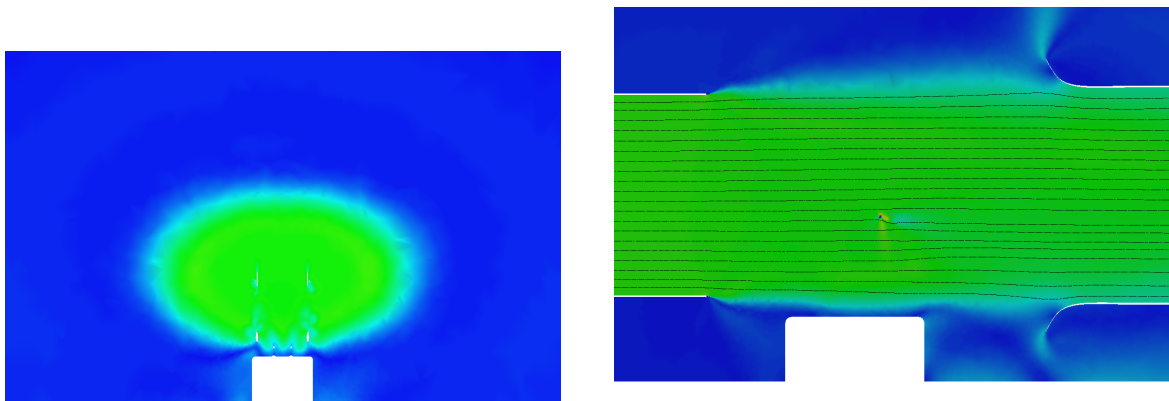


Fig. 18 Mach number for the WT case with no wing at station $x=0.172$ m and at span station $y=0.0$ m